

Tuning spatial entanglement in interacting few-electron quantum dots

Dung N. Pham,^{1,2} Sathwik Bharadwaj,^{1,2,*} and L. R. Ram-Mohan^{2,3,†}

¹*Department of Physics, Worcester Polytechnic Institute, Worcester, Massachusetts 01609.*

²*Center for Computational NanoScience, Worcester Polytechnic Institute, Worcester, Massachusetts 01609, USA.*

³*Departments of Physics, Electrical and Computer Engineering, and Mechanical Engineering, Worcester Polytechnic Institute, Worcester, Massachusetts 01609, USA.*

Confined geometries such as semiconductor quantum dots are promising candidates for fabricating quantum computing devices. When several quantum dots are in proximity, *spatial* correlation between electrons in the system becomes significant. In this article, we develop a fully variational action integral formulation for calculating accurate few-electron wavefunctions in configuration space, irrespective of potential geometry. To evaluate the Coulomb integrals with high accuracy, a novel numerical integration method using multiple Gauss quadratures is proposed. Using this approach, we investigate the confinement of two electrons in double quantum dots, and evaluate the spatial entanglement. We investigate the dependence of spatial entanglement on various geometrical parameters. We derive the two-particle wavefunctions in the asymptotic limit of the separation distance between quantum dots, and obtain universal saturation values for the spatial entanglement. Resonances in the entanglement values due to avoided level-crossings of states are observed. We also demonstrate the formation of electron clusters, and show that the entanglement value is a good indicator for the formation of such clusters. Further, we show that a precise tuning of the entanglement values is feasible with applied external electric fields.

Keywords: *spatial entanglement, quantum dots, Coulomb integrals, variational methods, qubits*

January 30, 2022

I. INTRODUCTION

Similarities can be drawn between the electronic properties of a single quantum dot and a hydrogenic atom, which implies that we can also develop an analogous Hund’s multiplicity rule [1, 2] for these artificial atoms [3–5]. When two or more quantum dots (QDs) are in the vicinity of one another, the system can be thought of as a covalent molecule of QDs [6]. Tunability in their inter-electron interaction with the separation distance and with external fields facilitates an enhanced level of control in their electronic properties [7–10]. Advances in the precise fabrication of QDs [11–13] have led to substantial improvements in the prospects of developing integrated devices for applications in quantum computing [14–20], quantum information [21, 22], and quantum memory circuits [23–25].

Evaluation and measurement of the entanglement in a multi-particle system has attracted extensive theoretical and experimental interest [26–31]. A complete description of a quantum system is given by a wavefunction that has both spin and spatial components. Hence the entanglement will also have contributions from spin and spatial correlations of the wavefunction. When QDs are in proximity, the spatial correlation between electrons in the system becomes significant and leads to the *spatial entanglement*. Such spatial entanglement will alter con-

siderably with changes in the geometrical parameters of QDs and with external perturbations.

The spatial entanglement properties are of interest to realize solid state all-electronic quantum computing devices. To this end, there have been several proposals to define deterministic teleportation protocols for quantum information processing in semiconducting nanowires [32], double QDs [33, 34], quantum dot arrays [35], and coupled quantum wires [36]. Applications of spatial entanglement as an indicator for bound and unbound states [37], as well as the effects of a magnetic field on entanglement have been discussed earlier [38]. The spatial entanglement properties in Helium and Helium-like atoms have been studied in the literature [39, 40]. Entanglement calculations for the ground state in simplistic models, such as the Hooke’s-atom model [41] and symmetric one-dimensional quantum wells with point-contact modeling for the Coulomb potential [42], have been considered. Recently, it has also been shown that the spatial overlapping of indistinguishable particles can be employed in quantum information processes through local measurements [43]. For all such applications it is important to fabricate the devices operating at the resonant entanglement values. A detailed study to obtain the “spectroscopy” of quantum entanglement in QDs has not been considered so far.

A thorough understanding of the spatial correlation of particles is also crucial to the fabrication and manipulation of charge qubits, which are usually coupled through the Coulomb interaction [44]. Although the literature on using charge qubits for quantum information purposes has been prolific [45, 46], there are surprisingly sparse theoretical studies on the entanglement that is intrinsic in the spatial wavefunctions describing the qubits. More specifically, how the spatial coupling between the parti-

* sathwik@wpi.edu

† LRRAM@wpi.edu

cles depends on the system, and on external parameters, is of great interest.

In this article, we consider the confinement of two electrons in QDs formed through nanowire heterostructures. Such structures have been considered as an ideal candidate for quantum electronic devices [47] and quantum information processes [48–50], since particles can be very effectively localized, either through external fields [50, 51] or by superlattice nanowires [52–56]. In either case the lateral width has negligible contributions to the entanglement properties. It is crucial to note that although in this study we consider specifically one-dimensional (1D) confinement for the particles, the methodology and conclusions are generalizable to any high-dimensional bipartite systems. In this article, we consider only the 1D potential confinements, and the generalization to higher dimensions will be presented elsewhere.

One well-studied approach for few-electron problems is the full configuration interaction (FCI) method, which uses a basis set constructed from single-particle orbitals. Due to its success as the benchmark for few-particle atomic and molecular calculations [57, 58], the FCI has been used in condensed matter setups [59–62]. In this study, we develop an alternative variational formalism for calculating the coordinate-space representation of the few-particle wavefunctions in semiconductor confinements. Accurate energy values and wavefunctions can be obtained through our geometry discretization scheme based on the principle of stationary action. We note that full scale FCI calculations with Schrodinger-Poisson self consistent single particle basis [64, 65], or with atomistic tight-binding basis [66, 67] are desirable for system with several electrons in quantum dots. Our method provides a useful pre-step before such large scale FCI for simulating new devices. It may also be used to benchmark FCI results [63]. We emphasize that our method is best suited to solve few-body confinement problems.

New results presented in this article are summarized below:

1. We have studied the case of two electrons trapped in different variations of a double QDs. We obtain the eigen-spectrum, and measure the spatial entanglement by computing the linear entropy of the system. We show that through geometrical manipulations of the confining potential and/or using external electric fields, one can tune the level of entanglement.
2. We derive exact representations for the wavefunctions in the asymptotic limit, and obtain universal saturation values for the entanglement.
3. Resonances in the *entanglement* are observed as a consequence of avoided level-crossings (also called anti-crossings) in the energy spectrum in an applied electric field, or with variations of the width in asymmetric double QDs. Electron cluster formations are also detected at the excited states, which lead to additional local maxima.

This paper is organized as follows: In Sec. II, we describe the variational scheme for solving the few-particle action integral. In Sec. III, the energy spectrum for two electrons in GaAs/Ga_xAl_{1-x}As symmetric double QDs are discussed. We also derive the asymptotic representations to explain the degeneracy spectrum. Spatial entanglement properties for the symmetric double QDs are discussed in Sec. IV. Entanglement resonances, and the two electron-cluster formation in a system of asymmetric QDs are studied in Sec. V. We analyze the effect of an applied electric field on the entanglement in Sec. VI. We obtain the entanglement values in the asymptotic separation distance in Appendix A. Calculation of the entanglement properties with parabolic dot confinement is given in Appendix B. Concluding remarks are given in Sec. VII.

II. VARIATIONAL FORMULATION FOR FEW-PARTICLE WAVEFUNCTIONS

Let us consider a two-electron wavefunction in configuration space written as

$$\Phi(x_1, \sigma_1, x_2, \sigma_2) = \psi(x_1, x_2)S(\sigma_1, \sigma_2), \quad (1)$$

where $\psi(x_1, x_2)$ and $S(\sigma_1, \sigma_2)$ are the spatial and the spin components of the wavefunction, respectively. Here, $x_1(\sigma_1)$ and $x_2(\sigma_2)$ represent the position (spin) coordinates of the electron 1 and 2, respectively. Within the envelope-function approximation [72], the spatial part of the charge carrier's envelope function $\psi(x_1, x_2)$ satisfies the time-independent Schrödinger's equation of the form

$$\left\{ -\frac{\hbar^2}{2} \left[\frac{d}{dx_1} \left(\frac{1}{m_1^*} \frac{d}{dx_1} \right) + \frac{d}{dx_2} \left(\frac{1}{m_2^*} \frac{d}{dx_2} \right) \right] + V(x_1, x_2) \right\} \psi = E\psi, \quad (2)$$

where $m_1^* \equiv m_1^*(x_1)$, $m_2^* \equiv m_2^*(x_2)$ are the effective masses of the two electrons, and $V(x_1, x_2)$ is the effective potential. $V(x_1, x_2)$ contains terms arising from the geometrical confinement of the system, V_0 , and the Coulomb interaction between the electrons. It is given by

$$V(x_1, x_2) = V_0(x_1) + V_0(x_2) + \frac{e^2}{4\pi\epsilon_0|x_1 - x_2|}. \quad (3)$$

We multiply Eq. (2) with $\delta\psi^*$, a small variation in the function ψ^* and integrate over all space Ω to obtain

$$\int_{\Omega} dx_1 dx_2 \delta\psi^* \left[-\frac{\hbar^2}{2} \left\{ \frac{d}{dx_1} \left(\frac{1}{m_1^*} \frac{d}{dx_1} \right) + \frac{d}{dx_2} \left(\frac{1}{m_2^*} \frac{d}{dx_2} \right) \right\} + V(x_1, x_2) - E \right] \psi = 0. \quad (4)$$

Using the integration by parts on the first two terms in the above integral we obtain

$$\begin{aligned} \delta \int_{\Omega} dx_1 dx_2 \left[\frac{\hbar^2}{2} \left(\frac{d\psi^*}{dx_1} \cdot \frac{1}{m_1^*} \frac{d\psi}{dx_1} + \frac{d\psi^*}{dx_2} \cdot \frac{1}{m_2^*} \frac{d\psi}{dx_2} \right) \right. \\ \left. + \psi^* (V(x_1, x_2) - E) \psi \right] \\ = \delta \int dx_1 dx_2 \mathcal{L}(x_1, x_2) = 0, \quad (5) \end{aligned}$$

where $\mathcal{L}(x_1, x_2)$ is identified as the two-particle Lagrangian density of the system. Hence, the action integral corresponding to Eq. (2) is given by

$$\begin{aligned} A &= \int dt \int_{\Omega} dx_1 dx_2 \mathcal{L}(x_1, x_2), \\ &= T \int_{\Omega} dx_1 dx_2 \left[\frac{\hbar^2}{2} \left(\frac{d\psi^*}{dx_1} \cdot \frac{1}{m_1^*} \frac{d\psi}{dx_1} + \frac{d\psi^*}{dx_2} \cdot \frac{1}{m_2^*} \frac{d\psi}{dx_2} \right) \right. \\ &\quad \left. + \psi^* (V(x_1, x_2) - E) \psi \right]. \quad (6) \end{aligned}$$

Since we are considering a steady-state problem, the time integral is simply a constant T . We are interested in finding bound states of the system, hence Dirichlet boundary conditions are imposed along the periphery of the truncated finite domain.

The domain Ω is discretized into a refined finite element mesh. A schematic for the discretization of a one-dimensional physical domain is shown in Fig. 1(a). In a bipartite problem, this discretization is applied to each particle's space x_1 and x_2 . This results in a 2N-dimensional finite element mesh, with N being the dimension of the particle confinement of the problem. For example, two electrons confined in a 1D physical space results in a 2D parameter space as shown in Fig. 1(b). Here x_1 and x_2 represents the coordinate of the first and second particle, respectively. Although in this paper we consider specifically electrons trapped in 1D geometry, the method is generalizable to any number of dimensions.

Within each 2N-dimensional parameter space element, the two-particle spatial wavefunction is represented as a linear combination of the interpolation polynomials $N_i(x_k)$ with as-yet undetermined coefficients ψ_{ij} , given by

$$\psi^{iel}(x_1, x_2) = \sum_{ij} \psi_{ij} N_i(x_1) N_j(x_2), \quad (7)$$

where iel is the element index, and ψ_{ij} are undetermined wavefunction values at nodes (vertices) of the element. In contrast to employing global basis functions, using a local element representation offers exceptional flexibility in obtaining accurate wavefunctions, since discretization can be done to systems of arbitrary shapes. In our calculation, we employ Hermite interpolation polynomials [73], in which the variational parameters are the wavefunction, and its first derivative values at each node. Using the

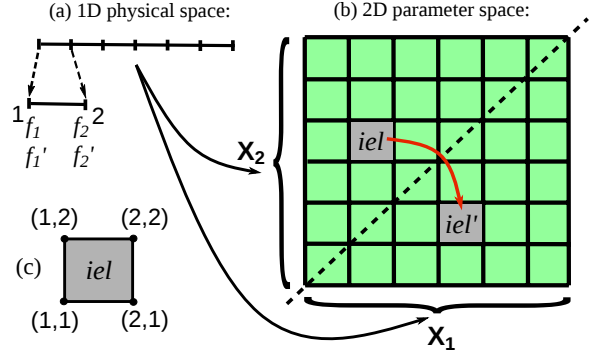


FIG. 1: (a) A schematic representation of the discretization in one dimension is shown. For Hermite interpolations, each node has coefficients corresponding to the wavefunction and its first derivative values. (b) A mapping of the 1D discretization into a 2D-parameter space (x_1, x_2) for a two-particle problem is shown. Elements iel and iel' are related through the mirror reflection across the mutual axis (represented by the dashed line). (c) A sample 2D element within which the wavefunction is represented using Eq. (7) is displayed.

Hermite interpolation polynomials guarantee the function and the first derivative continuity throughout the domain Ω .

To impose the antisymmetric property of fermions, the following scheme is used. Let iel be an element in the discretized parameter space. Since both particles share the same physical space, for a given element iel there exists a distinct element iel' related to it through the mirror reflection across the mutual axis of the parameter space (see Fig. 1(b)). For a spatial wavefunction to be symmetric (or antisymmetric), we demand that within iel' , the local representation satisfies the relation

$$\psi^{iel'}(x_1, x_2) = \pm \psi^{iel}(x_1, x_2) = \pm \sum_{ji} \psi_{ji} N_j(x_1) N_i(x_2), \quad (8)$$

where the \pm sign corresponds to a symmetric or antisymmetric spatial wavefunction, respectively. Note that this procedure also reduces the number of variational parameters by half, since the nodal values associated with iel' are now related to those of iel .

The action integral in Eq. (6) is then evaluated within each element using Eq. (7), and the total action is found by summing over all elements. In Fig. 1(c) we show an example of element in the 2D parameter space. Here the variational parameters are the wavefunction and their first derivative values that are corresponding to the vertices of the square element. A more detailed discussion of the finite element analysis and the Hermite interpolation polynomials can be found in Ref. [73–77].

Using the principle of stationary action, a variation of Eq. (6) with respect to Ψ^\dagger (a row vector containing all

variational parameters corresponding to the function ψ^*) results in a generalized eigenvalue problem of the form

$$(\mathbf{K} - E\mathbf{U})\Psi = 0, \quad (9)$$

where \mathbf{K} is the coefficient matrix corresponding to the first 3 terms in the two-particle Lagrangian density defined in Eq. (6), \mathbf{U} is the coefficient matrix associated with overlap integrals corresponding to the coefficient E in Eq. (6), and Ψ is the column vector containing all the nodal values to be determined. Once the nodal values are obtained by solving the generalized eigenvalue problem in Eq. (9), the wavefunction at any location can be calculated through reinterpolation using Eq. (7).

Being a variational method based on geometry discretization, the accuracy of our scheme in computing wavefunctions is geometry-independent and can be applied to QDs of any arbitrary shapes, with any desired level of accuracy achievable by suitable mesh refinement. In contrast to the traditional Raleigh-Ritz method, our scheme provides the necessary flexibility in the element-based trial wavefunctions, and more variational parameters in the form of nodal values of the wavefunction and its derivatives.

Within the scope of this paper, we consider strictly one-dimensional confinement, since the lateral effects are negligible for QDs formed through the nanowire heterostructures. The justification for the reduction of Coulomb integrals to one dimension is given in the supplementary material. We note that special attention is needed to evaluate the Coulomb contribution to the action integral since it has singularities at $x_1 = x_2$. We propose an efficient way to evaluate numerically such integrals using multiple orders for Gauss quadratures, and this is discussed in the supplementary material.

III. ENERGY CALCULATIONS FOR TWO-PARTICLE SYSTEMS

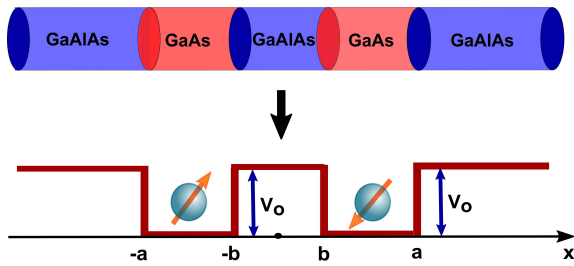


FIG. 2: Schematic of a one-dimensional double quantum dot system.

Consider a system of two electrons in the conduction band of a symmetric GaAs/Ga_xAl_{1-x}As double QDs. A realistic implementation of such a system can be a heterostructure nanowire composed of alternative layers of GaAs and GaAlAs stacked onto each other, as shown in Fig. 2. For a stoichiometric ratio $x = 0.37$ the potential depth is $V = 0.276$ eV, the effective mass of the electron $m_{in}^* = 0.0665 m_e$ inside, and $m_{out}^* = 0.0858 m_e$ outside the dots [78], where m_e is the rest mass of an electron. These material properties are considered for all calculations presented in this paper.

In Table I, eigenvalues of the first eight states in a symmetric double QD are presented for different separation distances d . We observe that as $d \rightarrow \infty$, we obtain 2- and 4-fold degeneracies. This can be explained as follows.

For two-electron systems, the simplest approximation of the spatial wavefunction is the traditional Slater determinant representation with single-particle wavefunctions, given by

$$|\psi_{\text{spatial}}\rangle = \begin{cases} \frac{1}{\sqrt{2}} [|a\rangle_1 |b\rangle_2 \pm |b\rangle_1 |a\rangle_2], & a \neq b; \\ |a\rangle_1 |a\rangle_2, & a = b, \end{cases} \quad (10)$$

where $|a\rangle$, $|b\rangle$ are the single-particle wavefunctions for the symmetric double QD potential, and the subscript is the particle index. The total wavefunction is given by $|\Psi\rangle = |\psi_{\text{spatial}}\rangle \otimes |S_{\text{spin}}\rangle$. Spatial wavefunctions in Eq. (10) are associated with the symmetric or antisymmetric spin parts $|S_{\text{spin}}\rangle$ so that the total wavefunction $|\Psi\rangle$ is antisymmetric under the exchange operator \hat{P} . Note that the above representation leads to only singlets (for $a = b$) and 2-fold degenerate states (for $a \neq b$). Moreover, the Slater determinant representation neglects the Coulomb interaction that is particularly important for QDs in proximity.

Here, we first give a representation which is accurate at the asymptotic limit of large separation distance d between the dots, and then explain the degeneracy pattern observed in Table. I. Let $\mathbb{S}(n, i) = \{ |n, \alpha\rangle_i \mid \alpha \in \mathbb{N} \}$, be the basis set for an electron in a single QD, where $n = 1, 2$ is the dot index, α is the single-particle quantum number, and $i = 1, 2$ is the particle index. In the asymptotic limit, the Hamiltonian commutes (i) with the exchange operator \hat{P} , which permutes the particle indices, and (ii) with \hat{W} , which permutes the dot indices. Also, as $d \rightarrow \infty$, the Coulomb interaction vanishes and the electrons are bound to one of the QDs with zero tunneling probability to the other dot. Hence we derive the spatial part of the wavefunction as linear combinations of the eigenstates of $\mathbb{S}(n, i)$ given by

(α, β)	$d \rightarrow \infty$	$d=30$ nm	$d=10$ nm	$d=6$ nm	$d=4$ nm	$d=0$ nm
(1, 1)	0.03381551453605	0.06597445297395	0.09117827187267	0.10132363931689	0.10766511883166	0.12308265436399
	0.03381551453605	0.06597445297393	0.09117827187810	0.10132363932279	0.10766511891643	0.12306768828638
(1, 2)	0.08413370110643	0.11633416555783	0.14217840394755	0.15312310251314	0.16020213212699	0.17196886060204
	0.08413370110643	0.11633416555779	0.14217840403115	0.15312310253815	0.16020213239190	0.17190045732112
	0.08413370110643	0.11704336845825	0.14608683015824	0.15918731650000	0.16777544459370	0.18441352939932
	0.08413370110643	0.11704336845822	0.14608683024372	0.15918731661314	0.16777544608388	0.18438741290837
(2, 2)	0.13445188767681	0.16741965485019	0.19756820520027	0.21209234809771	0.22187638627095	0.22786101607874
	0.13445188767681	0.16741965485014	0.19756820550444	0.21209234852245	0.22187639053093	0.22790743753463

TABLE I: Eigenvalues (measured in eV) of the first eight states of a symmetric double QD are tabulated for several separation distances d between the QDs. The width of each quantum dot is $w_1 = w_2 = 15$ nm. States are labeled with a pair of quantum numbers (α, β) . The Coulomb energy increases with decreasing distance as seen in the table.

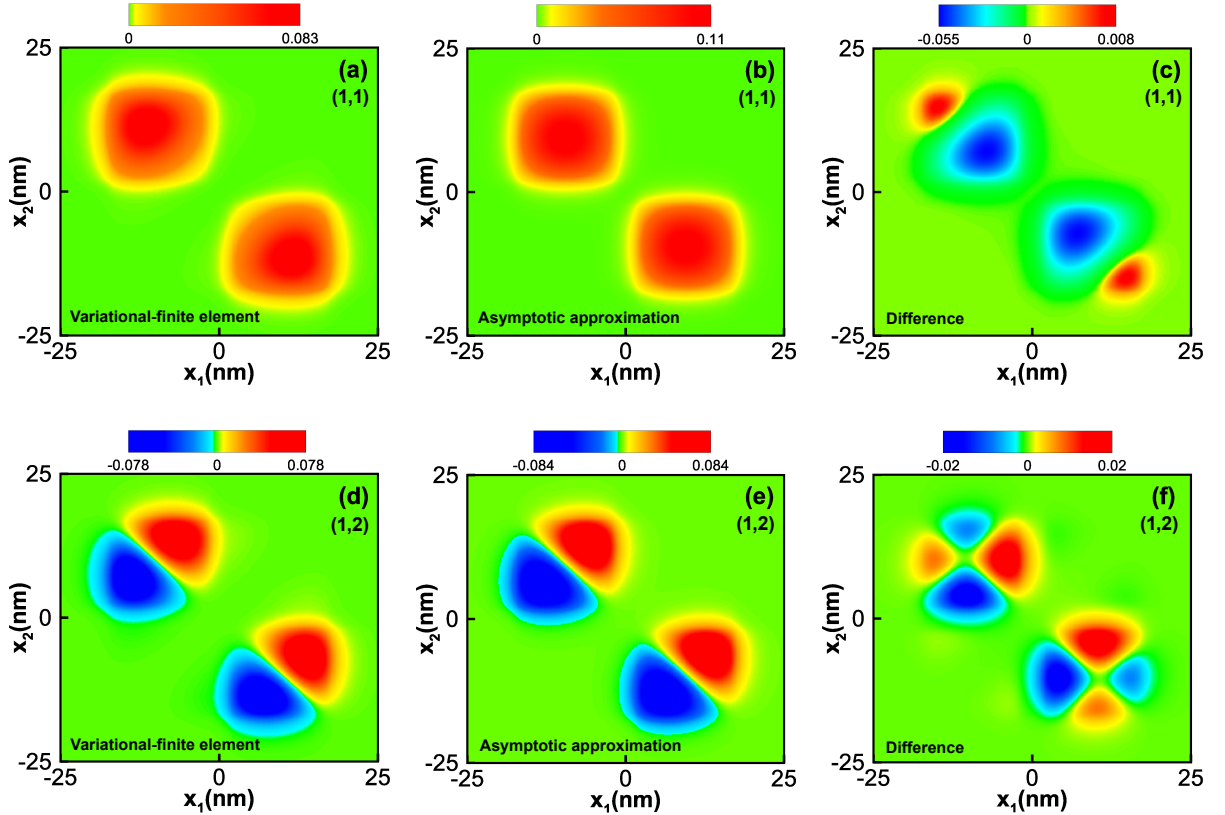


FIG. 3: Wavefunctions obtained through our method for the state (a) (1, 1), and (d) (1, 2) are shown for the separation distance $d = 4$ nm between the QDs. Wavefunctions obtained through the asymptotic representation in Eq. (11) for the state (1, 1) and (1, 2) are shown in (b) and (e), respectively. The difference between the two representations are plotted in (c) and (f). The width of each quantum dot is $w_1 = w_2 = 15$ nm.

$$|\psi_s^+\rangle = \frac{1}{2\sqrt{1+\delta_{\alpha\beta}}} \left[\left(|1, \alpha\rangle_1 |2, \beta\rangle_2 + |1, \beta\rangle_1 |2, \alpha\rangle_2 \right) + \left(|2, \alpha\rangle_1 |1, \beta\rangle_2 + |2, \beta\rangle_1 |1, \alpha\rangle_2 \right) \right]; \quad (11)$$

$$|\psi_s^-\rangle = \frac{1}{2} \left[\left(|1, \alpha\rangle_1 |2, \beta\rangle_2 - |1, \beta\rangle_1 |2, \alpha\rangle_2 \right) - \left(|2, \alpha\rangle_1 |1, \beta\rangle_2 - |2, \beta\rangle_1 |1, \alpha\rangle_2 \right) \right]; \quad (12)$$

$$|\psi_a^+\rangle = \frac{1}{2} \left[\left(|1, \alpha\rangle_1 |2, \beta\rangle_2 - |1, \beta\rangle_1 |2, \alpha\rangle_2 \right) + \left(|2, \alpha\rangle_1 |1, \beta\rangle_2 - |2, \beta\rangle_1 |1, \alpha\rangle_2 \right) \right]; \quad (13)$$

$$|\psi_a^-\rangle = \frac{1}{2\sqrt{1+\delta_{\alpha\beta}}} \left[\left(|1, \alpha\rangle_1 |2, \beta\rangle_2 + |1, \beta\rangle_1 |2, \alpha\rangle_2 \right) - \left(|2, \alpha\rangle_1 |1, \beta\rangle_2 + |2, \beta\rangle_1 |1, \alpha\rangle_2 \right) \right], \quad (14)$$

where $\hat{\mathcal{P}}|\psi_s^\pm\rangle = |\psi_s^\pm\rangle$, $\hat{\mathcal{P}}|\psi_a^\pm\rangle = -|\psi_a^\pm\rangle$, $\hat{\mathcal{W}}|\psi_s^\pm\rangle = \pm|\psi_s^\pm\rangle$, and $\hat{\mathcal{W}}|\psi_a^\pm\rangle = \pm|\psi_a^\pm\rangle$. As before, spatial wavefunctions in Eqs. (11)-(14) are associated with the symmetric or anti-symmetric spin parts $|S_{\text{spin}}\rangle$ so that $|\Psi\rangle$ is antisymmetric under the exchange operator $\hat{\mathcal{P}}$. If $\alpha \neq \beta$, then the four wavefunctions in Eqs. (11)-(14) form a set of four-fold degenerate states. If, on the other hand, $\alpha = \beta$ then Eqs. (12) and (13) vanish, resulting in a doublet.

For a finite distance d between the QDs, the Coulomb interaction splits these degeneracies, and the representations in Eqs. (11)-(14) are no longer exact. In Table. I, we have classified the eigenvalues in terms of the quantum numbers (α, β) . The representation $|\psi_s^+\rangle$, the accurate wavefunctions obtained from the technique described in Sec. II, and their difference for the quantum numbers (1,1) and (1,2) are plotted in Figs. 3(a)-3(f). From Figs. 3(c) and 3(f), we see that the disagreements are significant as a consequence of the Coulomb interaction, which impact on the amount of spatial entanglement. In the following section we calculate the entanglement in such double QDs, and discuss the observed resonances.

IV. SPATIAL ENTANGLEMENT IN QUANTUM DOTS

A. Formalism

Any state that describes a system of identical fermions has to obey the antisymmetry under the exchange operator. This makes the state necessarily nonseparable, and hence entangled. The lowest level of entanglement is provided by the use of single-particle states in a Slater determinant form of the wavefunction [79-85]. This level of entanglement may be thought of as a baseline with which a more complete calculation of the entanglement can be compared. In the following, we quantify entanglement by measuring the *linear entropy* of the system. It is known in the literature that the linear entropy is a good indicator of entanglement [29, 40, 41, 83, 84], and can be computed efficiently even for a very large Hilbert space. The linear entropy is defined as

$$\mathcal{E}_\ell = 1 - \text{Tr}(\rho_1^2), \quad (15)$$

where ρ_1 is the reduced density matrix. Here ρ_1 is obtained by taking the trace over the second particle

$$\rho_1 = \text{Tr}_2(\rho), \quad (16)$$

where ρ is the density matrix of the whole system. The spatial and spin components are separable, and the density matrix can be written as a tensor product of each contribution

$$\rho = \rho_{\text{spatial}} \otimes \rho_{\text{spin}}, \quad (17)$$

and

$$\text{Tr}(\rho_1^2) = \text{Tr}(\rho_{\text{spatial}}^2) \text{Tr}(\rho_{\text{spin}}^2). \quad (18)$$

Since the trace of the spin and spatial parts are entirely separable, we can consider them separately. For a two-electron system, the spin contributions are readily evaluated as

$$\text{Tr}(\rho_{\text{spin}}^2) = \begin{cases} 1, & |\uparrow\uparrow\rangle \text{ or } |\downarrow\downarrow\rangle \\ 0.5, & \frac{1}{\sqrt{2}} [|\uparrow\downarrow\rangle \pm |\downarrow\uparrow\rangle] \end{cases}. \quad (19)$$

Thus the contribution of the spin part to the total trace of ρ_1^2 is a constant. Hence, we lay it aside from our consideration of the spatial entanglement. In the following the spatial part of the density matrix is referred to as ρ , and we consider the measure of spatial entanglement to be

$$\begin{aligned} \mathcal{E}_\ell &= 1 - \text{Tr}(\rho_{\text{spatial}}^2) \\ &= 1 - \int_{-\infty}^{+\infty} \int_{-\infty}^{+\infty} |\langle \mathbf{r}'_1 | \rho | \mathbf{r}_1 \rangle|^2 d\mathbf{r}'_1 d\mathbf{r}_1. \end{aligned} \quad (20)$$

Electron distributions and the evolution of the spatial entanglement with varying parameters are found to be very analogous for symmetric and antisymmetric partners, and a detailed comparison of the entanglement properties of symmetric and antisymmetric states are given in the supplementary materials. Therefore, for further analysis in this paper, we only discuss the results for the symmetric states; the same conclusions can be drawn for the antisymmetric case.

B. Symmetric double quantum dot

In Figs. 4(a)–4(f), spatial entanglement of a double dot is plotted as a function of d . We observe that as $d \rightarrow \infty$, spatial entanglement \mathcal{E}_ℓ saturates to either 0.5 or 0.75. In fact, in the asymptotic limit we see that

$$\mathcal{E}_\ell = \begin{cases} 0.5, & \alpha = \beta \\ 0.75, & \alpha \neq \beta \end{cases} \quad (21)$$

as shown in Figs. 4(a)–4(f). This observation can be confirmed by computing analytically \mathcal{E}_ℓ with the asymptotic forms of the wavefunctions presented in Eqs. (11)–(14), as in Appendix A.

One can also interpret this result from a probabilistic point of view by considering the behavior of the bound states in a symmetric system of two indistinguishable particles. In the asymptotic limit, each particle is located in a different quantum dot, unaffected by the presence of the other particle. Then, states α and β describe separated electrons exactly. For $\alpha = \beta$, there is no ambiguity as to which single-particle state the particles are occupying. However, due to the indistinguishability of the electrons and the QDs being symmetrical, there is only 0.5 probability of where each particle is located – each electron can either be in QD 1 or 2, while the second electron is then in the other QD. This 0.5 certainty is reflected in the measurement of the entanglement. On the other hand, if $\alpha \neq \beta$, then there is an additional uncertainty; we not only have 50% information on where a particle is located, but also 50% on what state the particle is occupying in each dot (state α or β). Therefore, the amount of certainty is $0.5 \times 0.5 = 0.25$; the amount of entanglement is therefore $1 - 0.25 = 0.75$. Note that the interpretation and the asymptotic values of entanglement are valid for any type of quantum dot irrespective of dimensionality and geometry, as long as the two QDs are identical to each other. The lower bound of the spatial entanglement is observed to be 0.5. This is due to electrons being indistinguishable, and hence the wavefunction is an eigenfunction of the operator \hat{P} . However, if the electrons are distinguished through their spin directions then the overall entanglement vanishes.

In Figs. 4(a) – 4(c), we see that as $d \rightarrow \infty$, the entanglement values of the first three bound states monotonically reach the saturation values. The situation for higher states is more complex, as can be seen in Figs. 4(d) – 4(f). For states 3 and 5, the entanglement reaches a maximum, while for state 4 it drops to a minimum, before approaching the corresponding asymptotic values. Such extrema in the behavior of the entanglement are a result of two major competing effects in the system: (i) wavefunction overlapping, and (ii) the Coulomb repulsion. As the QDs are brought into proximity, single-particle wavefunctions of the two electrons localized in these dots can overlap each other. At the same time, the repulsive Coulomb interaction between the electrons becomes stronger at closer distances and opposes such overlap of

the wavefunctions. The influence of these effects is visible for entanglement values of excited states (states 3, 4 and 5), where a larger probability of finding the electron is distributed outside the QDs. Then the wavefunction of one electron is susceptible to interactions with the wavefunction of the electron in the neighboring QD. Due to these competing effects, the entanglement of the system develops extremal points, indicating a switch in the roles of the two effects. When the QDs are placed far apart, both the Coulomb interaction and the overlap of single-electron wavefunctions become insignificant, and the entanglement reaches a saturation value at the asymptotic limit.

V. ASYMMETRIC SYSTEMS

In this section we discuss how asymmetry in the configuring potential affects the entanglement. Consider a system of asymmetric double QDs, in which the width of the first QD is fixed at 15 nm, and the width of the second QD is varied. The distance between the QDs is held constant at 10 nm. The entanglement of the ground state and the next eight excited states as a function of the second QD's width w_2 are plotted in Figs. 5(a)–5(i). In Fig. 5(a), we see that there is only a small variation in the amount of entanglement of the ground state with w_2 . This is because both electrons are in the ground state, and the change in w_2 will not lead to any interaction with the higher energy levels. In other words, the electron distribution and the entanglement values are not perturbed significantly with changing w_2 due to the strong electron confinement within each QD.

Effects of asymmetry are substantially more significant for the excited states. When the potential has a mirror symmetry, we observe resonances in the entanglement values for some excited states labeled by M_1 , M_2 , M_4 , M_5 , and M_6 in Fig. 5. For example, as soon as the symmetry is broken either by increasing or decreasing w_2 , the entanglement for the first excited state drops rapidly from 0.75 to 0.5 (see Fig. 5(b)). This is due to QDs no longer being identical, hence the ambiguity in assigning single-particle states is removed. This effect can be seen clearly in the evolution of the wavefunction of the first excited state as the dot width w_2 is varied. As shown in Fig. 6(a), when the potential is symmetric ($w_1 = w_2 = 15$ nm), the wavefunction is an eigenstate of both the exchange operators \hat{P} and \hat{W} as discussed in Sec. III. When the symmetry is broken, the wavefunction is only an eigenstate of \hat{P} (see Fig. 6(b)), and the asymptotic representation is now given by

$$|\phi^\pm\rangle = \frac{1}{\sqrt{2}}(|1, \alpha\rangle_1 |2, \beta\rangle_2 \pm |2, \beta\rangle_1 |1, \alpha\rangle_2). \quad (22)$$

Note that in the above equation, the index α and β are now specifically assigned to QD 1 and 2, respectively.

Since the states that an electron can have is fixed depending on which QD it is confined, the ambiguity in

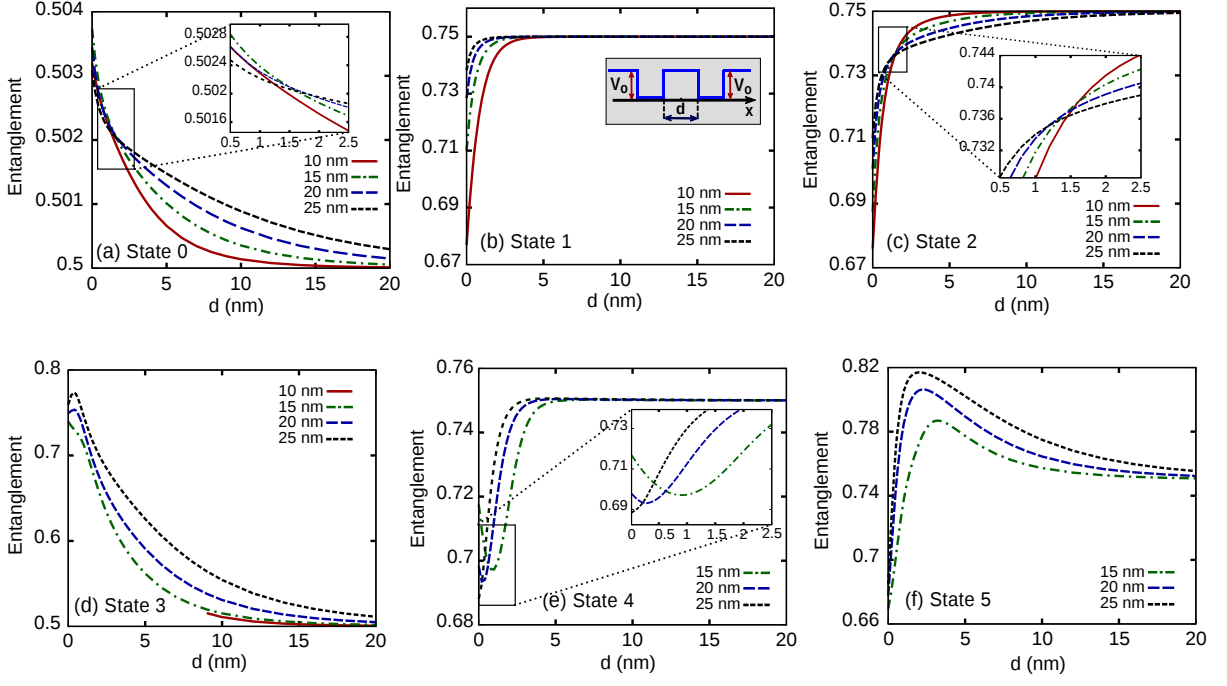


FIG. 4: Spatial entanglement for the first five eigenstates of two electrons in a symmetric double QD system is plotted as a function of separation distance d , for four different widths of the QDs: 10 nm, 15 nm, 20 nm, and 25 nm. The entanglement values saturate to either 0.5 or 0.75 in the limit $d \rightarrow \infty$.

choosing between α and β is removed, thereby dropping the entanglement value from 0.75 towards 0.5. Similar behavior (see Figs. 5(c), 5(e)-5(i)) can be seen in any state whose asymptotic value for the entanglement saturation is 0.75 in the case of symmetric QDs.

A. Entanglement resonances due to avoided level-crossings

In Fig. 5, we observe several entanglement resonances even when $w_1 \neq w_2$. These resonances are due to avoided level-crossings of the eigenstates. For example, in Fig. 5(c) and (d), we observe an entanglement resonance labeled as R_{23} at $w_2 = 28.43$ nm for the 2nd and 3rd excited state, respectively. This is due to the interaction between adjacent states 2 and 3 which undergo an avoided level-crossing at R_{23} . After the resonance, wavefunctions for these two adjacent states evolve into one another. In Fig. 7, we have plotted the wavefunction for state 2 and 3 before, at, and after the resonance R_{23} . We observe that the wavefunction of state 2 (Fig. 7(a)) transforms into that of state 3 (Fig. 7(c)) after the resonance, and vice versa. Around R_{23} , wavefunctions of both these states are heavily deformed due to maximal interaction between these adjacent states, as seen in Figs. 7(b) and 7(e). Such inter-mixing results in a high level of entanglement. Similar mechanisms will explain rest of the resonances labeled as R_{ij} , which indicate the interaction between the excited states i and j . For instance, the resonance R_{34} shown in

Fig. 5(d) and (e) is due to avoided level-crossing between the excited states 3 and 4. Also, since asymmetry in the system can be created both by increasing or decreasing w_2 , similar resonances are observed on either side of the symmetric width $w_2 = 15$ nm.

Eigenvalues for the first nine bound states are plotted as a function of w_2 in Fig. 8. Avoided level-crossings are seen at the entanglement resonance positions R_{ij} that are observed in Fig. 5. We note that around $w_1 = w_2$, the spectrum is almost doubly degenerate due to the mirror symmetry of the system. This is distinct from the avoided-crossings observed in the asymmetric systems.

B. Electron cluster formation

A special case of avoided level-crossing occurs when accompanied with the formation/dissolution of electron clusters, and are observed as additional maxima in the entanglement values. We can tune the width, separation distance, and the potential depth of the QDs so that the two electrons are in the same quantum dot, forming a “cluster.” Such two-electron clusters can also be formed at higher excited states of double QDs. In Fig. 9(a) we have shown an occurrence of a two-electron cluster in the 7th excited state for a system of symmetric double QDs. We see that the cluster has an equal probability distribution across both QDs due to mirror symmetry of the potential. However, in case of asymmetric QDs, this mirror symmetry is lost. As seen in Fig. 9(b), the cluster

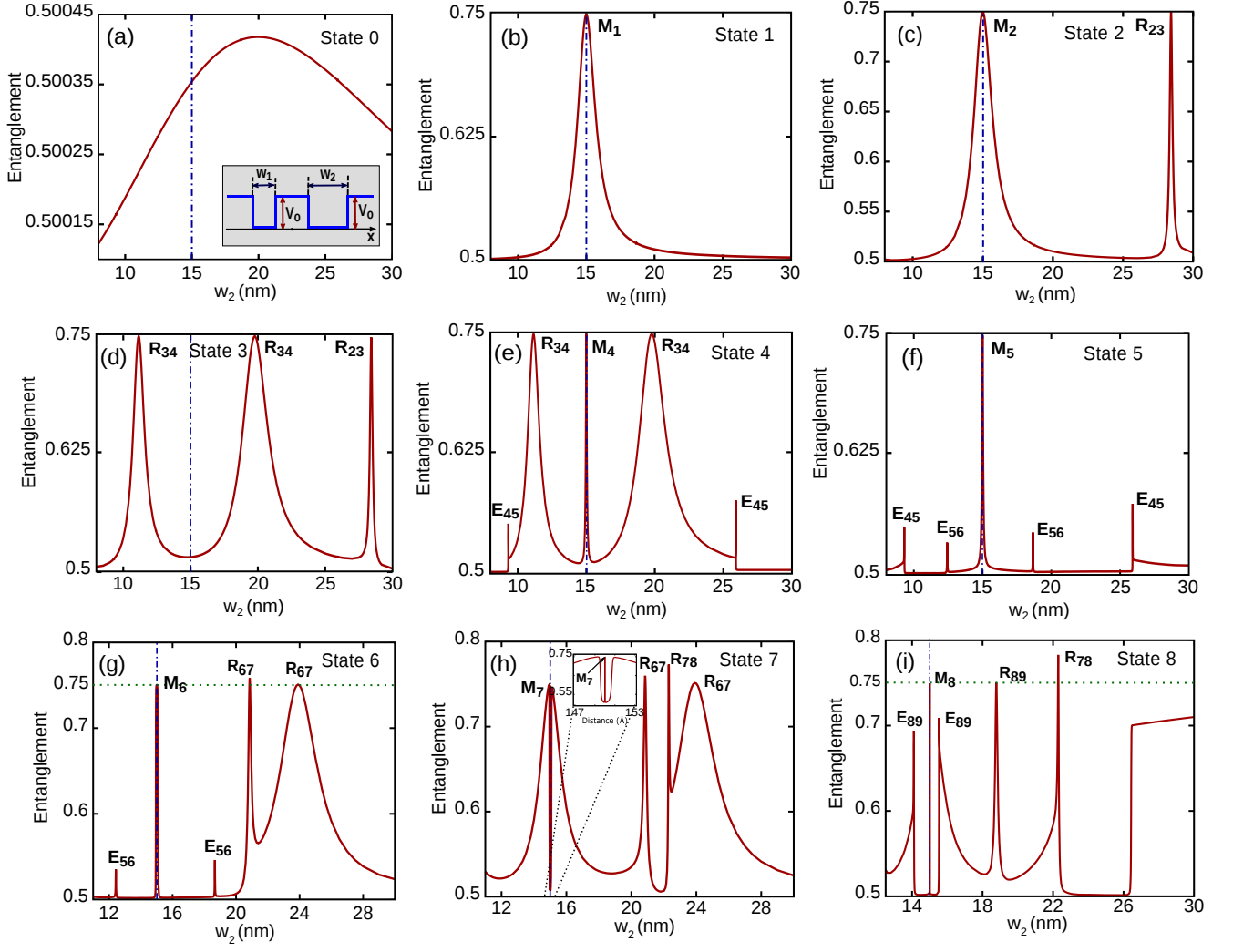


FIG. 5: Spatial entanglement values for the first 8 eigenstates of two electrons in a non-symmetric double QD are plotted as a function of width of the second QD w_2 (see inset in (a)). Width of the first QD is $w_1 = 15$ nm, and kept constant for all calculations. The distance between the QDs is $d = 10$ nm. Here, the resonance peaks (i) M_i are due to the mirror symmetry of the system, (ii) R_{ij} are due to avoided level-crossings (anti-crossings) between states i and j , and (iii) E_{ij} are due to the formation/dissolution of electron clusters.

will occupy only QD 2 out of the two QDs.

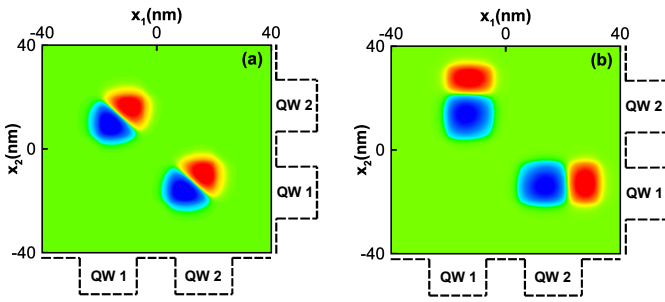


FIG. 6: Wavefunctions of the first excited state are plotted for: (a) a symmetric system ($w_1 = w_2$) and (b) when the symmetry is broken ($w_1 \neq w_2$). Axes x_1 and x_2 are the coordinates of 1st and 2nd electron.

To elaborate further, we note that the x_1 - (x_2 -) axis represents the position of the first (second) electron. Following the potential pattern of the QDs in Fig. 9(a), we see that both electrons have probability distribution in either of QDs. This is in contrast with, for example Fig. 6, where we see that if the first electron is in the first QD, then the second electron will be in the second QD, and vice versa. Formation of such two-electron clusters leads to additional resonances in the spatial entanglement. These resonances are classified into two categories: (1) resonance due to mirror symmetry of the potential, (2) local maxima due to the evolution of two separate electrons into a two-electron cluster, and vice versa.

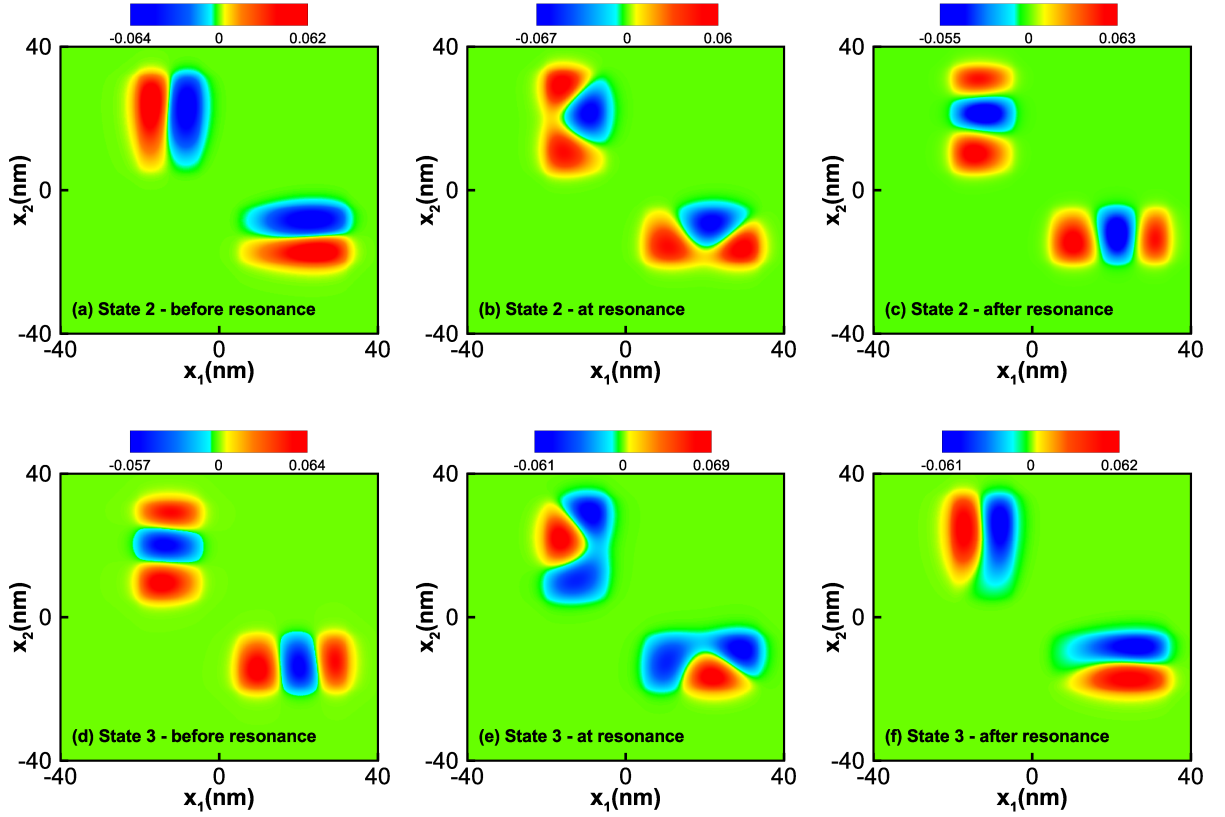


FIG. 7: Wavefunctions of the second and third excited states are plotted before, at, and after the resonance R_{23} , observed in Fig. 5(c).

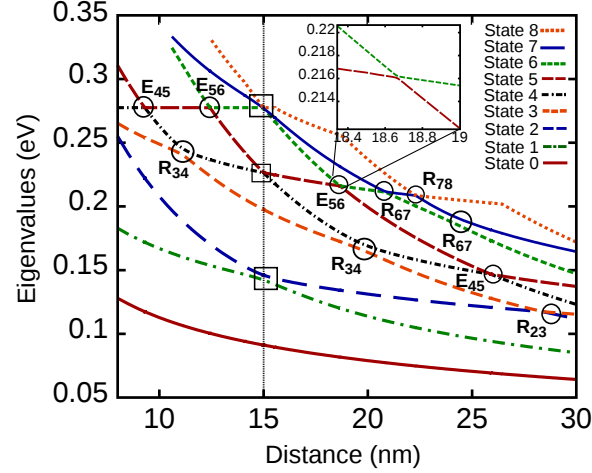


FIG. 8: Eigenvalues of the first 9 bound states are plotted as function of w_2 . Resonances corresponding to avoided level-crossings are marked by circles, while splittings due to symmetry breaking are marked by squares. An instance of avoided level crossing is shown in the inset. R_{ij} and E_{ij} are the labels corresponding to the resonance peaks observed in Fig. 5.

1. Resonance due to mirror symmetry of the potential

We have observed that the 7th and 8th excited states have an electron cluster occupancy. For example, this is seen for the 7th state in Fig. 9. In Figs. 5(h) and 5(i), we

have plotted the entanglement values for these states as a function of the second dot width w_2 . We see that breaking the mirror symmetry of the system while going away from the symmetric dot width $w_2 = 15$ nm, the entanglement value drops from 0.75 to 0.5. These resonances

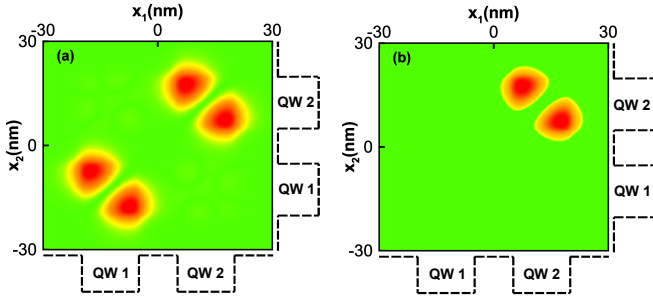


FIG. 9: Wavefunctions of the 7th excited state when (a) the QDs are identical, $w_1 = w_2 = 150$ nm, and (b) when symmetry is broken with $w_1 = 150$ nm, $w_2 = 150.03$ nm are plotted.

are labeled as M_7 , and M_8 in Figs. 5(h) and 5(i), respectively. This can be explained as follows: when the electron cluster is in a single QD for the case of $w_1 \neq w_2$, the entanglement value \mathcal{E}_l is close to 0.5. For $w_1 = w_2$, the probability of finding the electron cluster is distributed equally in each QD, and this will contribute an additional 50% uncertainty in the particle occupation within either dot. Hence, we observe an increase in the entanglement value to 0.75.

2. Transition between two separate electrons to a two-electron cluster

In the case of asymmetric double QDs, the electron cluster can be formed at lower energies. Transition between a state with two separate electrons to a two-electron cluster can be deduced through the occurrence of local resonance maxima in the entanglement. In Figs. 5(e), 5(f), and 5(g), such resonances are labeled as E_{45} and E_{56} , which indicates the avoided-level crossings between the neighboring states 4 and 5, and 5 and 6, respectively. In Fig. 8, we have shown these crossings between the eigenvalues.

Wavefunctions for the excited states 4 and 5 around the resonance E_{45} are plotted in Figs. 10(a)-10(f). After the resonance E_{45} , the two-electron cluster occupancy is favored over the single electron localization within each QD. Hence it occurs at a lower energy. Therefore, the sharp peak at E_{45} occurs along with the formation/dissolution of electron clusters as displayed in Fig. 10. For example, in Fig. 5(e), state 4 has two separate electrons in each QDs before the resonance E_{45} . Whereas, after the resonance, the state 4 will have a two-electron cluster occupancy. Analogous mechanisms explain the resonance E_{56} in Fig. 5(f), where we see that after the resonance the state 5 has a two-electron cluster occupancy.

VI. RESONANCES IN ENTANGLEMENT WITH APPLIED EXTERNAL ELECTRIC FIELDS

In this section, we study the entanglement properties in symmetric double QDs with an applied constant electric field \mathbf{E} . The additional term in the Hamiltonian is given by

$$H'(x) = |e|Ex. \quad (23)$$

The “ramp” potential breaks the mirror symmetry of the system. The entanglement of the two electrons as a function of $\Delta V = |e|Ed$ is shown for the 3rd, 4th, and 5th states in Figs. 11(a)-11(c).

Although the mechanism for creating asymmetry is different, phenomena similar to the case of the asymmetric QDs, discussed in Sec. V, are observed. Spatial Entanglement in states with $\alpha \neq \beta$ decreases rapidly with the applied electric field (see Figs. 11(b), 11(c)), and resonant behavior associated with avoided level-crossings are also present (see Figs. 11(a)-11(c)). Electron cluster formation occurs with the applied field as the QD potential profile is tilted. In Figs. 11(a) and 11(b), the sharp resonance peak F_{34} is formed due to the avoided level-crossing between the state with two separate electrons (state 3), and the state that corresponds to an electron cluster (state 4). A similar mechanism explains the formation of the entanglement resonance F_{45} in Figs. 11(b) and 11(c), which is formed due to multiple avoided level-crossings between the states 4 and 5.

Since one can vary the magnitude of the field with reasonable ease in experiments, the occupancy of electrons in each QD can be controlled and varied effectively by external electric fields without having to re-fabricate the width of QDs. Moreover, since resonances associated with transitions from a double to a single occupancy (and vice versa) are extremely sharp, entanglement measurement is an excellent indicator for the electron cluster formation/dissolution.

Sensitivity of the system to small changes in symmetry facilitates the use of very small electric fields to initiate the formation of electron clusters, given that the system is already near the resonance due to the inherent asymmetry in the potential profile. This can be done by designing two QDs having different widths in such a way that the system is close to a resonance, and a weak electric field can then initiate this transition. The process can be reversed efficiently by reversing the direction of the electric field. To illustrate this, consider the resonance E_{56} in Fig. 5(f). The width w_1 of the first QD is 15 nm, and $w_2 = 18.6$ nm. Now instead of achieving the resonance by slowly increasing w_2 , we have introduced a small E-field. The change in entanglement of the system by varying the magnitude of \mathbf{E} is shown in Fig. 12. As can be noted from the range of the x -axis label in Fig. 12, due to the built-in asymmetry of the system, the required electric field to reach resonance, and hence to create an electron cluster, is substantially reduced.

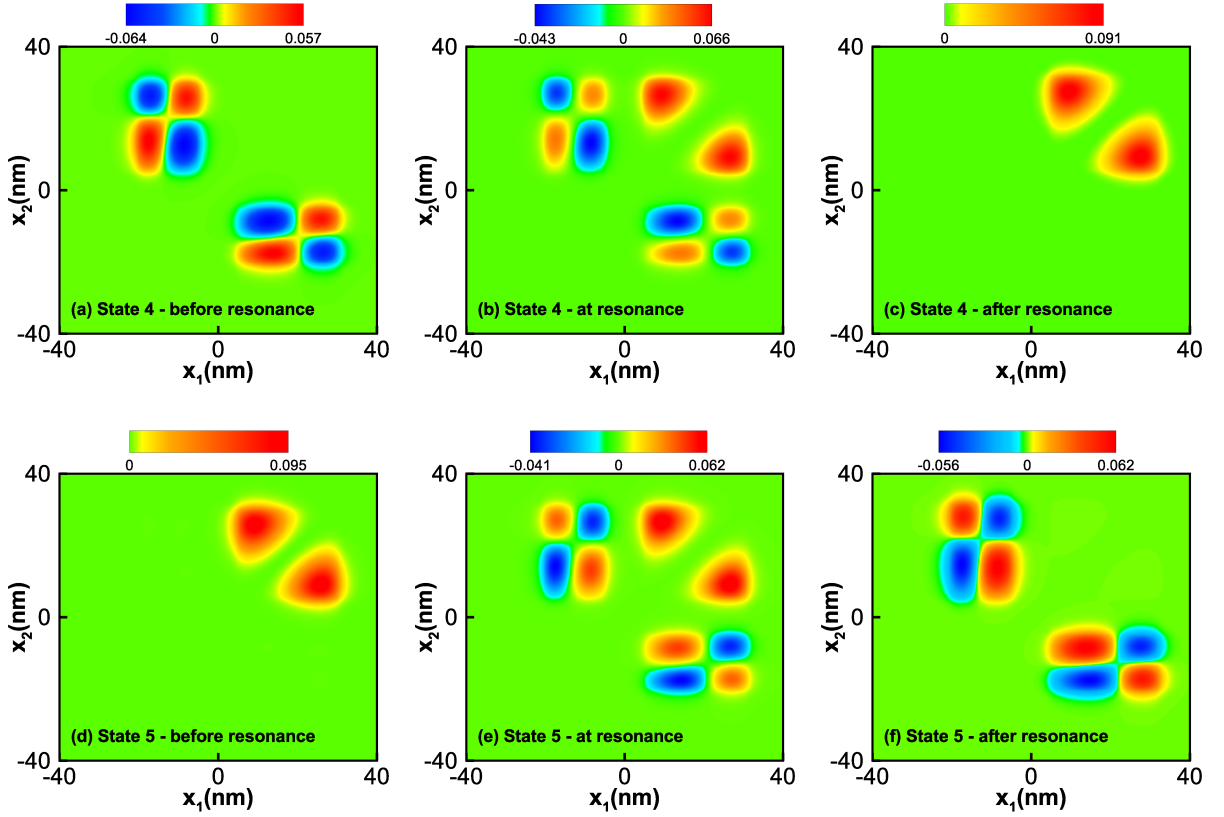


FIG. 10: Wavefunctions of the forth and fifth excited states are plotted before, at, and after the resonance E_{45} , observed in Fig. 5.

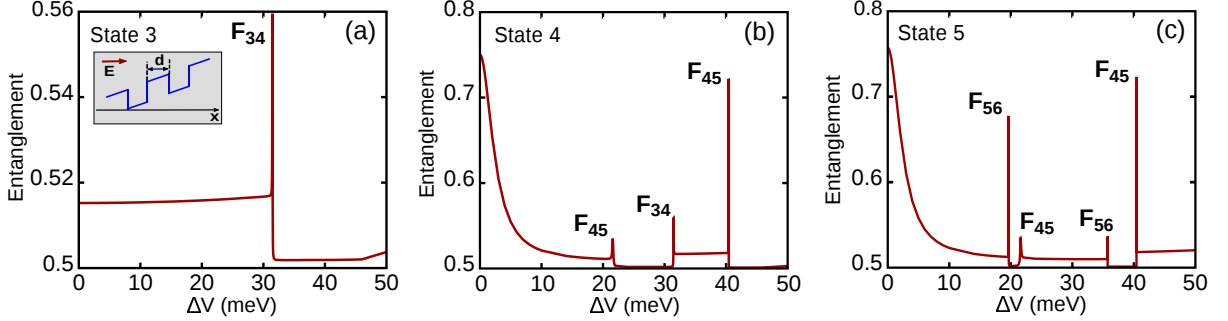


FIG. 11: Spatial entanglement of excited states 3, 4, and 5 for two electrons in a symmetric double QDs is plotted as a function of applied potential ΔV . The distance between QDs are kept constant at 10 nm, and the width $w_1 = w_2 = 15$ nm. Here, the peak F_{ij} corresponds to an avoided level-crossing between the excited states i and j .

VII. CONCLUDING REMARKS

We have developed a variational formalism for calculating the coordinate-space representation for the few-particle wavefunctions. Finite-element discretization based on the principle of stationary action provides an accurate eigen-spectrum for any complex geometry. Singularities arising while evaluating the Coulomb integral are circumvented using multiple Gauss quadrature of different orders. Our scheme can be easily extended to study few-electron quantum confinements in higher dimensions

for any complicated potential distribution.

We obtained the solutions for two-electrons in double QDs, and studied the spatial entanglement properties of their wavefunctions. We investigated the dependence of the energy spectrum and the spatial entanglement on various geometrical parameters. We derived exact asymptotic wavefunctions to explain the degeneracy spectrum, and universal saturation values for the spatial entanglement as separation distance $d \rightarrow \infty$. These saturation values were found to be 0.5 for quantum numbers $\alpha = \beta$, and 0.75 for $\alpha \neq \beta$.

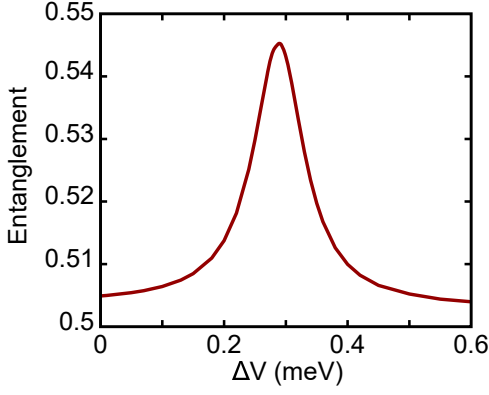


FIG. 12: Spatial entanglement of state 5 for two electrons in an asymmetric double QDs is plotted as a function of applied potential ΔV . The dot widths are $w_1 = 15$ nm, $w_2 = 18.6$ nm, and the separation distance is $d = 10$ nm.

We observed resonances in the entanglement values for the first time in both symmetric and asymmetric QDs. These entanglement resonances are found as a consequence of (a) breaking the mirror symmetry of the potential, (b) avoided level-crossings between the excited states, or (c) due to the interaction between states supporting single-electron and the two-electron clusters. We note that the spatial entanglement value is a good indicator for the formation and dissolution of such electron clusters.

Further, we showed that a precise tuning of the entanglement values is feasible with an applied electric field. Since the magnitude of the external field can be tuned readily in experiments, the occupancy of electrons in each QD can be controlled and varied effectively. Our results dictate that when several QDs are in proximity, spatial correlation between electrons in the system becomes significant. The ability to tune the entanglement values with external parameters unveils new avenues for forming and manipulating quantum bits.

In this article, we have focused on the theory of spatial entanglement in QDs. Preliminary work on quantum wires and the two electron spatial entanglement in them shows very similar trends. These studies of spatial entanglement will be reported separately in the near future.

VIII. ACKNOWLEDGMENTS

We thank P. K. Aravind for valuable discussions. DNP thanks Worcester Polytechnic Institute for summer undergraduate research fellowships. Part of the calculations presented here were performed using computational resources supported by the Academic and Research Computing Group at WPI.

Appendix A: Entanglement in double QDs in the asymptotic limit

In this Appendix, we show the spatial entanglement, \mathcal{E}_ℓ , for a symmetric double QD as $d \rightarrow \infty$. In the asymptotic limit, the two-particle states are represented by one of the four wavefunctions in Eqs. (11)–(14). Here we calculate \mathcal{E}_ℓ for Eq. (11), but similar results can be derived for the other three representations. The reduced density matrix for $|\psi_s^+\rangle$ in Eq. (11) is given by

$$\begin{aligned} \rho_1 &= \frac{1}{4(1 + \delta_{\alpha\beta})} \int \langle \mathbf{r}_2 | \psi_s^+ \rangle \langle \psi_s^+ | \mathbf{r}_2 \rangle d\mathbf{r}_2 \\ &= \frac{1}{4(1 + \delta_{\alpha\beta})} \int \left(\langle \mathbf{r}_2 | 2, \beta \rangle_2 | 1, \alpha \rangle_1 + \langle \mathbf{r}_2 | 2, \alpha \rangle_2 | 1, \beta \rangle_1 \right. \\ &\quad \left. + \langle \mathbf{r}_2 | 1, \beta \rangle_2 | 2, \alpha \rangle_1 + \langle \mathbf{r}_2 | 1, \alpha \rangle_2 | 2, \beta \rangle_1 \right) \\ &\quad \times \left(\langle 2, \beta | \mathbf{r}_2 \rangle_2 \langle 1, \alpha |_1 + \langle 2, \alpha | \mathbf{r}_2 \rangle_2 \langle 1, \beta |_1 \right. \\ &\quad \left. + \langle 1, \beta | \mathbf{r}_2 \rangle_2 \langle 2, \alpha |_1 + \langle 1, \alpha | \mathbf{r}_2 \rangle_2 \langle 2, \beta |_1 \right) d\mathbf{r}_2. \end{aligned} \quad (\text{A1})$$

Then

$$\begin{aligned} \rho_1 &= \frac{1}{4(1 + \delta_{\alpha\beta})} \left[|1, \alpha \rangle \langle 1, \alpha| + |1, \beta \rangle \langle 1, \beta| + |2, \alpha \rangle \langle 2, \beta| \right. \\ &\quad \left. + |2, \beta \rangle \langle 2, \beta| + \delta_{\alpha\beta} \left(|1, \alpha \rangle \langle 1, \beta| + |1, \beta \rangle \langle 1, \alpha| \right. \right. \\ &\quad \left. \left. + |2, \alpha \rangle \langle 2, \beta| + |2, \beta \rangle \langle 2, \alpha| \right) \right]. \end{aligned} \quad (\text{A2})$$

In the above expression, the indices are dropped on the bras and kets, since all of them correspond to the first electron. The trace $\text{Tr}(\rho_1^2)$ gives

$$\begin{aligned} \text{Tr}(\rho_1^2) &= \int |\langle \mathbf{r}'_1 | \rho_1 | \mathbf{r}_1 \rangle|^2 d\mathbf{r}'_1 d\mathbf{r}_1 \\ &= \frac{1}{16(1 + \delta_{\alpha\beta})^2} \int \left| \langle \mathbf{r}'_1 | 1, \alpha \rangle \langle 1, \alpha | \mathbf{r}_1 \rangle + \langle \mathbf{r}'_1 | 1, \beta \rangle \langle 1, \beta | \mathbf{r}_1 \rangle \right. \\ &\quad \left. + \langle \mathbf{r}'_1 | 2, \alpha \rangle \langle 2, \alpha | \mathbf{r}_1 \rangle + \langle \mathbf{r}'_1 | 2, \beta \rangle \langle 2, \beta | \mathbf{r}_1 \rangle \right. \\ &\quad \left. + \delta_{\alpha\beta} \left(\langle \mathbf{r}'_1 | 1, \alpha \rangle \langle 1, \beta | \mathbf{r}_1 \rangle + \langle \mathbf{r}'_1 | 1, \beta \rangle \langle 1, \alpha | \mathbf{r}_1 \rangle \right. \right. \\ &\quad \left. \left. + \langle \mathbf{r}'_1 | 2, \alpha \rangle \langle 2, \beta | \mathbf{r}_1 \rangle + \langle \mathbf{r}'_1 | 2, \beta \rangle \langle 2, \alpha | \mathbf{r}_1 \rangle \right) \right|^2 d\mathbf{r}'_1 d\mathbf{r}_1. \end{aligned} \quad (\text{A3})$$

Note that we have the relation

$$\langle i, \alpha | j, \beta \rangle = \delta_{ij} \delta_{\alpha\beta}, \quad (\text{A4})$$

since single-particle states α and β are orthonormal, and bound-state wavefunctions of one QD do not overlap with the other in the asymptotic limit. Therefore, with some rearrangements the expression in Eq. (A3) is given by

$$\text{Tr}(\rho_1^2) = \begin{cases} 0.5, & \alpha = \beta \\ 0.25, & \alpha \neq \beta \end{cases} \quad (\text{A5})$$

Hence the amount of entanglement is given by

$$\mathcal{E}_\ell = 1 - \text{Tr}(\rho_1^2) = \begin{cases} 0.5, & \alpha = \beta \\ 0.75, & \alpha \neq \beta, \end{cases} \quad (\text{A6})$$

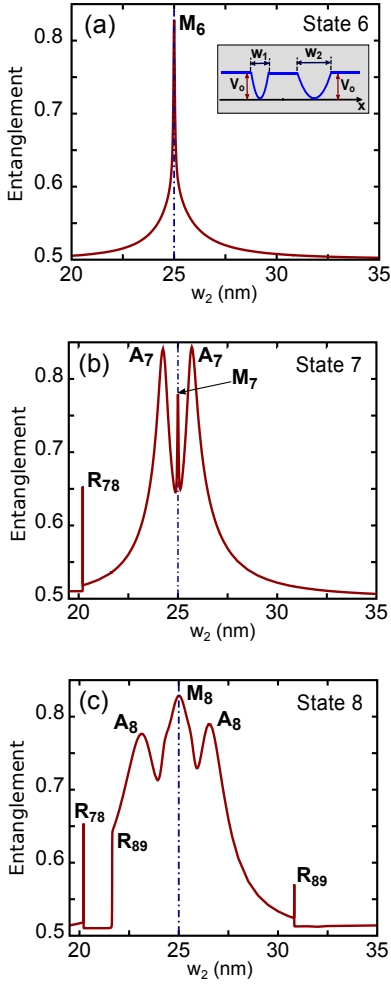


FIG. 13: Spatial entanglement for the excited states 6, 7, and 8 are plotted for asymmetric double parabolic QDs as a function of w_2 . The width w_1 is kept constant at 25 nm. Here, the resonance peaks (i) M_i are due to the mirror symmetry of the system, (ii) R_{ij} are due to avoided level-crossings between states i and j , and (iii) A_i are due transition between different mode numbers.

which is consistent with the qualitative probabilistic arguments presented in Sec. IV B.

Appendix B: Parabolic finite quantum dots

In this Appendix, we investigate the spatial entanglement in double parabolic QDs. The depth of each QD is chosen to be 276 meV, the width w_1 is fixed at 25 nm, and the width w_2 of the second QD is varied. The spatial entanglements for a selected number of excited states are shown in Figs. 13(a)-13(c). Avoided level-crossings are observed at the resonance positions R_{78} and R_{89} , as

shown in Figs. 13 and 14. Resonances due to breaking of the mirror symmetry of the potential are observed at M_6 , M_7 , and M_8 , located at $w_2 = 25$ nm as shown in Fig. 13.

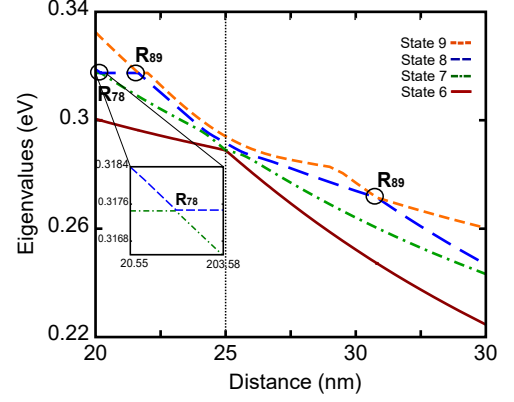


FIG. 14: Eigenenergies for two electrons in double parabolic QDs are plotted as a function of width of the second dot, w_2 . The first dot width is given by $w_1 = 25$ nm, and dot depths are 276 meV. Avoided level crossings are observed at R_{78} and R_{89} , and their resonance peaks can be seen in Fig. 13.

However, unlike in rectangular finite dots, here in parabolic dots there are many additional entanglement maxima that are not associated with any crossing of states. These maxima are labeled by A_i with i being the state index, such as A_7 and A_8 , as can be seen in Fig. 13. In double parabolic QDs, if the Coulomb interaction is absent, the eigenenergy $E \sim (n\omega_1 + m\omega_2)$, where (n, m) are mode numbers, and ω_1, ω_2 are angular frequencies. We can achieve the same eigenenergy through different choices of mode numbers (n, m) . Around these resonances we observe transitions between different choices of mode numbers (n, m) , and their intermixing leads to maxima in the entanglement. For example, at resonance A_7 the transition occurs between modes $(0, 3)$ and $(1, 2)$.

In Fig. 15, we plot the entanglement values for selected states in a symmetric double parabolic dot as a function of applied potential ΔV . We observe several avoided level-crossings (see inset in Fig. 15) that are manifested through a stepwise behavior in the entanglement values. These stepwise transitions are labeled as T_{ij} . The labeling T_{ij} represents the interactions between states i and j . For example, before resonance T_{45} , state 4 has an entanglement value that is close to 0.5, and the state 5 has value close to 0.75. Whereas, after the avoided level-crossing between state 4 and 5, their entanglement values are interchanged to have a stepwise behavior in the case of parabolic QDs. These characteristics may find applications in designing quantum bits, where the entanglements can be tuned through an external electric field.

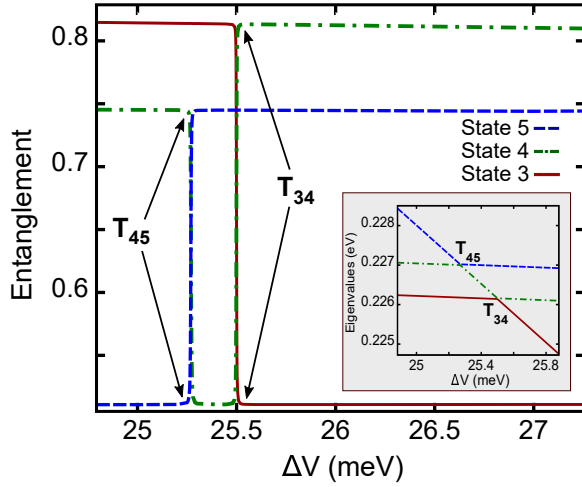


FIG. 15: Spatial entanglement of excited states in symmetric double parabolic QDs in an external electric field is plotted as a function of the applied potential ΔV . The step-wise transitions in the entanglement are due to the avoided level crossing between the adjacent states.

-
- [1] F. Hund, Z. Phys. **33**, 345–371 (1925); **34**, 296–308 (1925).
- [2] I. N. Levine, *Quantum Chemistry*, 5th ed. (Prentice Hall, New Jersey, 2000).
- [3] O. Steffens, U. Rossler, and M. Suhrke, Europhys. Lett. **42**, 529–534 (1998).
- [4] K. Keren, A. Stern, and U. Sivan, Eur. Phys. J. B **18**, 311–318 (2000).
- [5] Y. Sajeev, M. Sindelka, and N. Moiseyev, J. Chem. Phys. **128**, 061101 (2008).
- [6] X. Hu and S. Das Sarma, Phys. Rev. A **61**, 062301–1–19 (2000).
- [7] S. L. Chuang, *Physics of Optoelectronic Devices* (Wiley, New York, 1995).
- [8] M. Balkanski and R. F. Wallis, *Semiconductor Physics and Applications* (Oxford University Press, New York, 2000).
- [9] H. Haug, and S. W. Koch, *Quantum Theory of the Optical and Electronic Properties of Semiconductors*, 5th ed. (World Scientific Publishing Company, Singapore, 2009).
- [10] P. Michler (editor), *Quantum Dots for Quantum Information Technologies* (Springer, Switzerland, 2017).
- [11] M. Heiss, Y. Fontana, A. Gustafsson, G. Wüst, C. Magen, D. D. O’Regan, J. W. Luo, B. Ketterer, S. Conesa-Boj, A. V. Kuhlmann, J. Houel, E. Russo-Averchi, J. R. Morante, M. Cantoni, N. Marzari, J. Arbiol, A. Zunger, R. J. Warburton, and A. Fontcuberta i Morral, Nature Mater. **12**, 439–444 (2013).
- [12] K. Eng, T. D. Ladd, A. Smith, M. G. Borselli, A. A. Kiselev, B. H. Fong, K. S. Holabird, T. M. Hazard, B. Huang, P. W. Deelman, I. Milosavljevic, A. E. Schmitz, R. S. Ross, M. F. Gyure, and A. T. Hunter, Sci. Adv. **1**, e1500214–1–7 (2015).
- [13] N. W. Hendrickx, D. P. Franke, A. Sammak, M. Kouwenhoven, D. Sabbagh, L. Yeoh, R. Li, M. L. V. Tagliaferri, M. Virgilio, G. Capellini, G. Scappucci, and M. Veldhorst, Nat. Commun. **9**, 2835–1–7 (2018).
- [14] D. Loss, and D. P. DiVincenzo, Phys. Rev. A **57**, 120–126 (1998).
- [15] G. Burkard, D. Loss, and D. P. DiVincenzo, Phys. Rev. B **59**, 2070–2078 (1999).
- [16] T. Hayashi, T. Fujisawa, H. D. Cheong, Y. H. Jeong, and Y. Hirayama, Phys. Rev. Lett. **91**, 226804–1–4 (2003).
- [17] M. D. Shulman, O. E. Dial, S. P. Harvey, H. Bluhm, V. Umansky, A. Yacoby **336**, 6078–202–205 (2012).
- [18] Z. Shi, C. B. Simmons, D. R. Ward, J. R. Prance, X. Wu, T. S. Koh, J. K. Gamble, D. E. Savage, M. G. Lagally, M. Friesen, S. N. Coppersmith, and M. A. Eriksson, Nat. Commun. **5**, 3020–1–5 (2014).
- [19] D. Awschalom, N. Samarth, D. Loss (editors), *Semiconductor Spintronics and Quantum Computation* (Springer, Heidelberg, 2002).
- [20] M. E. Flatté, *Semiconductor Spintronics for Quantum Computation*, in *Manipulating Quantum Coherence in Solid State Systems*, p. 1–45 (Springer, Dordrecht, Netherlands, 2007).
- [21] N. C. Jones, R. V. Meter, A. G. Fowler, P. L. McMahon, J. Kim, T. D. Ladd, and Y. Yamamoto, Phys. Rev. X **2**, 031007–1–27 (2012).
- [22] M. R. Delbecq, T. Nakajima, P. Stano, T. Otsuka, S. Amaha, J. Yoneda, K. Takeda, G. Allison, A. Ludwig, A. D. Wieck, and S. Tarucha, Phys. Rev. Lett. **116**, 046802–1–6 (2016).
- [23] T. F. Watson, S. G. J. Philips, E. Kawakami, D. R. Ward, P. Scarlino, M. Veldhorst, D. E. Savage, M. G. Lagally, Mark Friesen, S. N. Coppersmith, M. A. Eriksson, and L. M. K. Vandersypen, Nature **555**, 633–637 (2018).
- [24] C. Berger, U. Huttner, M. Mootz, M. Kira, S. W. Koch,

- J.-S. Tempel, M. Aßmann, M. Bayer, A. M. Mintairov, and J. L. Merz, *Phys. Rev. Lett.* **113**, 093902–1–5 (2014).
- [25] Y. Li, G. W. Holloway, S. C. Benjamin, G. A. D. Briggs, J. Baugh, and J. A. Mol, *Phys. Rev. B* **96**, 075446–1–9 (2017).
- [26] J. Schliemann, J. Cirac, M. Kuś, M. Lewenstein, and D. Loss, *Phys. Rev. A* **64**, 022303–1–9 (2001).
- [27] H. Barnum, E. Knill, G. Ortiz, R. Somma, and L. Viola, *Phys. Rev. Lett.* **92**, 107902–1–4 (2004).
- [28] K. Eckert, J. Schliemann, D. Bruss, and M. Lewenstein, *Ann. Phys. (NY)* **299**, 88–127 (2002).
- [29] P. Zanardi, *Phys. Rev. A* **65**, 042101–1–5 (2002).
- [30] H. Wiseman and J. Vaccaro, *Phys. Rev. Lett.* **91**, 097902–1–4 (2003).
- [31] M. A. Nielsen, and I. L. Chuang, *Quantum Computation and Quantum Information* (Cambridge University Press, Cambridge, England, 2000).
- [32] H. Wang and S. Kais, *Chem. Phys. Lett.* **421**, 338–342 (2006).
- [33] R. L. de Visser and M. Blaauboer, *Phys. Rev. Lett.* **96**, 246801, 1–4 (2006).
- [34] A. G. Adepoju, B. J. Falaye, G.-H. Sun, O. C.-Nieto, and S.-H. Dong, *Laser Phys.* **27** 035201, 1–5 (2017).
- [35] F. de Pasquale, G. Giorgi, and S. Paganelli, *Phys. Rev. Lett.* **93**, 120502, 1–4 (2004).
- [36] F. Buscemi, P. Bordone, and Andrea Bertoni, *Phys. Rev. B* **81**, 045312, 1–6 (2010).
- [37] A. Ferrón, O. Osenda, and P. Serra, *Phys. Rev. A* **79**, 032509–1–6 (2009).
- [38] N. S. Simonovic, and R. G. Nazmitdinov, *Phys. Rev. A* **92**, 052332–1–19 (2015).
- [39] J. S. Dehesa, T. Koga, R. J. Yanez, A. R. Plastino, and R. O. Esquivel, *J. Phys. B* **45**, 015504–1–5 (2012); **45**, 239501 (2012).
- [40] Y.-C. Lin, C.-Y. Lin, and Y. K. Ho, *Phys. Rev. A* **87**, 022316–1–5 (2013).
- [41] J. P. Coe, A. Sudbery, and I. D’Amico, *Phys. Rev. B* **77**, 205122–1–14 (2008).
- [42] S. Abdullah, J. P. Coe, and I. D’Amico, *Phys. Rev. B* **80**, 235302–1–9 (2009).
- [43] R. L. Franco, and G. Compagno, *Phys. Rev. Lett.* **120**, 240403–1–6 (2018).
- [44] K. D. Petersson, C. G. Smith, D. Anderson, P. Atkinson, G. A. C. Jones, and D. A. Ritchie, *Phys. Rev. Lett.* **103**, 016805 (2009).
- [45] P. Bonderson and R. M. Lutchyn, *Phys. Rev. Lett.* **106**, 130505 (2011).
- [46] G. Cao, H. Li, T. Tu, L. Wang, C. Zhou, M. Xiao, G. Guo, H. Jiang, G. Guo, *Nat. Commun.* **4**, 1401 (2013).
- [47] E. D. Minot, F. Kelkensberg, M. van Kouwen, J. A. van Dam, L. P. Kouwenhoven, V. Zwiller, M. T. Borgström, O. Wunnicke, M. A. Verheijen, and E. P. A. M. Bakkers, *Nano Lett.* **7**, 2–367–371 (2007).
- [48] S. Nadj-Perge, S. M. Frolov, E. P. A. M. Bakkers, and L. P. Kouwenhoven, *Nature* **468**, 1084–1087 (2010).
- [49] P. Szumniak, J. Pawłowski, S. Bednarek, and D. Loss, *Phys. Rev. B* **92**, 035403 (2015).
- [50] S. Nadj-Perge, V. S. Pribiag, J. W. G. van den Berg, K. Zuo, S. R. Plissard, E. P. A. M. Bakkers, S. M. Frolov, and L. P. Kouwenhoven, *Phys. Rev. Lett.* **108**, 166801 (2012).
- [51] C. Fasth, A. Fuhrer, L. Samuelson, Vitaly N. Golovach, and Daniel Loss *Phys. Rev. Lett.* **98**, 266801 (2007).
- [52] M. S. Gudixsen, L. J. Lauhon, J. Wang, D. C. Smith, and C. M. Lieber, *Nature* **415**, 617–620 (2002).
- [53] M. T. Björk, B. J. Ohlsson, T. Sass, A. I. Persson, C. Thelander, M. H. Magnusson, K. Deppert, L. R. Wallenberg, and L. Samuelson, *Appl. Phys. Lett.* **80**, 1058 (2002).
- [54] Y. Wu, R. Fan, and P. Yang, *Nano Lett.* **2**, 2–83–86 (2002).
- [55] M. T. Björk, B. J. Ohlsson, T. Sass, A. I. Persson, C. Thelander, M. H. Magnusson, K. Deppert, L. R. Wallenberg, and L. Samuelson, *Nano Lett.* **2**, 2–87–89 (2002).
- [56] M. T. Björk, C. Thelander, A. E. Hansen, L. E. Jensen, M. W. Larsson, L. R. Wallenberg, and Lars Samuelson, *Nano Lett.* **4**, 9–1621–1625 (2004).
- [57] T. Abe, P. Maris, T. Otsuka, N. Shimizu, Y. Utsuno, and J. P. Vary, *Phys. Rev. C* **86**, 054301 (2012).
- [58] I. M. Savukov, *Phys. Rev. A* **93**, 022511 (2016).
- [59] Bhalchandra S. Pujari, Kavita Joshi, D. G. Kanhere, and S. A. Blundell *Phys. Rev. B* **78**, 125414 (2008).
- [60] S. A. Blundell and K. Joshi, *Phys. Rev. B* **81**, 115323 (2010).
- [61] J. J. Shepherd, G. Booth, A. Gruneis, and A. Alavi, *Phys. Rev. B* **85**, 081103(R) (2012).
- [62] R. M. Abolfath, and P. Hawrylak, *J. Chem. Phys.* **125**, 034707 (2006).
- [63] E. Nielsen and R. P. Muller, *A configuration interaction analysis of exchange in double quantum dots*, [arXiv:1006.2735](https://arxiv.org/abs/1006.2735) (2010).
- [64] X. Gao, E. Nielsen, R. P. Muller, R. W. Young, A. G. Salinger, N. C. Bishop, and M. S. Carroll, *15th International Workshop on Computational Electronics*, Madison, WI, 1–4 (2012).
- [65] X. Gao, E. Nielsen, R. P. Muller, R. W. Young, A. G. Salinger, N. C. Bishop, and M. S. Carroll, *J. of Appl. Phys.* **114**, 164302 (2013).
- [66] A. Tankasala, J. Salfi, J. Bocquel, B. Voisin, M. Usman, G. Klimeck, M. Y. Simmons, L. C. L. Hollenberg, S. Rogge, and R. Rahman *Phys. Rev. B* **97**, 195301 (2018).
- [67] Y. Wang, A. Tankasala, L. C. L. Hollenberg, G. Klimeck, M. Y. Simmons, R. Rahman *Npj Quantum Inf.* **2**, 16008 (2016).
- [68] L. R. Schwarz, G. H. Booth, and A. Alavi, *Phys. Rev. B* **91**, 045139 (2015).
- [69] P. M. Zimmerman, *J. Chem. Phys.* **146**, 104102 (2017).
- [70] A. A. Holmes, N. M. Tubman, and C. J. Umrigar, *J. Chem. Theory Comput.* **12**, 3674–3680 (2016).
- [71] Z. Wang, Y. Li, and J. Lu, *J. Chem. Theory Comput.* **15**, 3558–3569 (2019).
- [72] G. Bastard, *Phys. Rev. B* **24**, 5693 (1981); **25**, 7584 (1982); also see L. R. Ram-Mohan, K. H. Yoo, and R. L. Aggarwal, *ibid.* **38**, 6151 (1988), and references therein.
- [73] L. R. Ram-Mohan, *Finite Element and Boundary Element applications in Quantum Mechanics* (Oxford University Press Inc., New York, 2002).
- [74] O. C. Zienkiewicz and Y. K. Cheung, *Finite Element Methods in Structural and Continuum Mechanics* (McGraw-Hill, New York, 1967); O. C. Zienkiewicz, *The Finite Element Method* (McGraw-Hill, New York, 1977).
- [75] J. Jin, *The Finite Element Method in Electromagnetics*, 2nd ed. (Wiley, New York, 2002).
- [76] G. Dhatt, and G. Touzot, *The Finite Element Method Displayed* (Wiley, Lewiston, New York, 1984).
- [77] R. Goloskie, J. W. Kramer, and L. R. Ram-Mohan, *Comput. Phys.* **8**, 679–686 (1994).

- [78] I. Vurgaftman, J. R. Meyer, and L. R. Ram-Mohan, J. Appl. Phys., **89**, 5815–5875 (2001).
- [79] T. Ichikawa, T. Sasaki, I. Tsutsui, and N. Yonezawa, Phys. Rev. A **78**, 052105–1–8 (2008).
- [80] J. Schliemann, D. Loss, and A. MacDonald, Phys. Rev. B **63**, 085311–1–8 (2001).
- [81] G. Ghirardi, and L. Marinatto, Phys. Rev. A **70**, 012109–1–10 (2004).
- [82] N. Killoran, M. Cramer, and M. Plenio, Phys. Rev. Lett. **112**, 150501–1–6 (2014).
- [83] A. Plastino, D. Manzano, and J. Dehesa, Europhys. Lett. **86**, 20005–1–5 (2009).
- [84] F. Buscemi, P. Bordone, and A. Bertoni, Phys. Rev. A **75**, 032301–1–7 (2007).
- [85] J. Naudts and T. Verhulst, Phys. Rev. A **75**, 062104–1–9 (2007).